



Influence of NaNbO_3 on the structural, optical and dielectric properties of $0.05(\text{K}_{0.5}\text{Bi}_{0.5}\text{TiO}_3)\text{--}0.95(\text{NaNbO}_3)$ composites ceramics

S. K. Mohanty^{1,6} · Hari Sankar Mohanty² · Banarji Behera³ · Debi. P. Datta⁴ · S. Behera⁵ · Piyush R. Das⁶ 

Received: 3 August 2018 / Accepted: 4 February 2019 / Published online: 19 February 2019
© Springer Science+Business Media, LLC, part of Springer Nature 2019

Abstract

A new polycrystalline lead-free $0.05(\text{K}_{0.5}\text{Bi}_{0.5}\text{TiO}_3)\text{--}0.95(\text{NaNbO}_3)$ (KBT–NN) composites ceramics have been prepared by solid-state reaction method and their structural, optical, dielectric, ferroelectric and impedance properties are investigated. X-ray diffraction and Rietveld refinement data reveal that this composites ceramics possesses a perovskite-type orthorhombic structure after the diffusion of $\text{K}_{0.5}\text{Bi}_{0.5}\text{TiO}_3$ into the NaNbO_3 . An appreciable change in its vibrational phonon modes of KBT on addition of NaNbO_3 is exhibited in the material as observed from Fourier-transform infrared spectroscopy (FT-IR) spectrum. The optical band gap energy of the sample is determined from the diffused absorbance spectra to be 3.2 eV, which may be useful in photo-catalytic application. In the frequency range of $130\text{--}900\text{ cm}^{-1}$, different vibrational modes are observed from Raman spectrum. Field emission scanning electron microscopy (FE-SEM) images reveal a well-defined and homogeneous morphology. Polarization vs. electric field study confirms the ferroelectricity. Dielectric and complex impedance spectroscopic studies are performed over a wide range of frequency (i.e., $10^3\text{--}10^6\text{ Hz}$) and temperature ($30^\circ\text{--}500^\circ\text{ C}$) and it is found that Jonscher's power law is well applicable to the alternating current (*ac*) conductivity spectrum. The direct current (*dc*) conductivity of the material, which depends upon temperature, exhibits the decrease resistance with increase of temperature similar to that of semiconductors. The *dc* conductivity confirms that the conduction mechanism is influenced by oxygen vacancies.

1 Introduction

Lead based perovskite oxides have been the most prominent candidate of ferroelectric material due to their excellent dielectric and ferroelectric properties, ease of processing, and low cost. These materials are the complex perovskite oxides containing two cation species in which different charges are

randomly distributed on the A/B site of the ABO_3 structure [1–4]. The dielectric and ferroelectric properties in the complex perovskite is strongly modified by A/B site cation for which these materials establish their superiority over many others from application point of view. Out of all the studied ferroelectric oxides, only lead based ferroelectric oxides such as $\text{Pb}(\text{Zr},\text{Ti})\text{O}_3$ (PZT) and PZT-based multi-component ceramics are applied to various solid state devices. Unfortunately, they produce environmental pollutions because of the toxic nature [5]. To overcome this problems, lead free ferroelectric materials are synthesized for applications in devices [6]. Several kind of lead-free ferroelectric ceramics such as NBZT [7], $\text{Na}_{0.5}\text{Bi}_{0.5}\text{TiO}_3$ (NBT) [8], BNBLTZ [9] are developed. So far lead-based ferroelectric system is concerned, Pb^{2+} has its lone pair effect of 6s valence shell electron for which it exhibits high polarization. It is pertinent to mention here that Bi^{3+} possesses similar electronic configuration as Pb^{2+} , which motivates scientific community to develop the NBT based ceramics in the place of lead-based material. Potassium Bismuth Titanate $\text{K}_{0.5}\text{Bi}_{0.5}\text{TiO}_3$ (KBT), a perovskite structured material crystallized into tetragonal structure, exhibits a second order phase transition

✉ Piyush R. Das
prdas63@gmail.com; prdas_phy@vssut.c.in

¹ Department of Physics, M.H.D. College, Chhatia, Jajpur, Odisha, India

² Department of Physics & Astronomy, National Institute of Technology, Rourkela, Odisha, India

³ School of Physics, Sambalpur University, Burla, Odisha, India

⁴ Silicon Institute of Technology, Silicon Hill, Patia, Bhubaneswar, Odisha, India

⁵ Department of Physics, School of Applied Science, CUTM, Bhubaneswar, Odisha, India

⁶ Department of Physics, Veer Surendra Sai University of Technology, Burla, Odisha, India

(ferroelectric) with a relatively high Curie temperature (~ 380 °C). KBT is synthesized using different techniques [10–12]. Despite large remnant polarization (P_r) of $22.2 \mu\text{C}/\text{cm}^2$ and high Curie temperature ($T_c \sim 380$ °C) of KBT, problem appears in polling process due to high conductivity and large coercive field (E_c). To eradicate this problem, other ferroelectric materials, such as NBT-BT [13], Mn doped NBT-KBT [14], NKBT [15], NBT-KBT [16] are developed.

In comparison to ferroelectric materials, anti-ferroelectric materials exhibit better dielectric properties and high energy-storage density as reported [17]. NaNbO_3 (NN) having an orthorhombic distorted perovskite structure, exhibits anti-ferroelectric property at room temperature [18]. Because of its ability to undergo successive phase transitions, it attracts the attention of a number of researchers to synthesize NN-based lead-free systems [19]. Consequently, the investigation on structural and dielectric characteristics of NN-based materials such as $\text{NaNbO}_3\text{-ATiO}_3$ ($A = \text{Ba, Ca, Sr}$) [20–23], $\text{NaNbO}_3\text{-BaSnO}_3$ [24], $\text{NaNbO}_3\text{-Li SbO}_3$ [25] are carried out.

A solid solution of anti-ferroelectric and ferroelectric material usually results the formation of a new material. It reflects good ferroelectric and piezoelectric behavior. Hence, it is expected that the addition of KBT on NN can enrich the ferroelectric properties. Structural, dielectric and ferroelectric properties of KBT-NN solid solutions are reported [26]. The electrical properties and relaxation processes in the materials are obtained using impedance spectroscopy (IS). In this technique, analysis is done from the ac response to a sinusoidal perturbation. At different temperatures, the impedance and related parameters are calculated as a function of frequency [27]. The Curie temperature of ferroelectric materials has also been calculated from ac conductivity analysis [28]. From the literature survey, it is found that the electrical, optical properties and conduction mechanism in $0.05(\text{KBT})\text{-}0.95(\text{NN})$ are not studied using impedance spectroscopy. Therefore, in the present paper, we investigate the influence of NaNbO_3 on the structural, optical and dielectric properties of $0.05(\text{K}_{0.5}\text{Bi}_{0.5}\text{TiO}_3)\text{-}0.95(\text{NaNbO}_3)$ composites. We prepare $0.05(\text{KBT})\text{-}0.95(\text{NN})$ sample by taking all the ingredients at a time using stoichiometry, which is not done till date, to the best of our knowledge. Our study exhibits better structural and electrical properties of the sample.

2 Experimental details

The solid solution of $0.05(\text{KBT})\text{-}0.95(\text{NN})$ was synthesized via solid-state reaction method taking precursor materials: K_2CO_3 (> 99.9%), Na_2CO_3 (> 99.9%), TiO_2 (> 99.9%) (M/s. Merck Specialties Pvt. Ltd., Mumbai, India), Bi_2O_3 (> 99.9%) (Central Drug House Pvt. Ltd., New Delhi) and, Nb_2O_5 (> 99.9%) (M/s Finar Chemicals

Pvt. Ltd., Ahmadabad, India) in proper stoichiometry. The precursor materials were mixed thoroughly in air using an agate mortar for 2 h. Subsequently, adding methanol, the mixture was grinded for 2 h to have a homogenous mixture. Thermal cycle is as follows; first 300 °C is attained in 2 h, this temperature is maintained for 0.5 h, then the temperature is increased to 600 °C in 2 h and kept for 30 min at this temperature. Then temperature increased to 900 °C by 2 h, keeping 30 min in this temperature and finally raised to 1115 °C in 2 h. At this temperature, this mixture is placed for 4 h and the mixture is calcinated. The cylindrical pellets of diameter 12 mm and thickness 1–2 mm were compacted using hydraulic press at an isostatic pressure of $3.6 \times 10^6 \text{ N/m}^2$, taking polyvinyl alcohol as binder, followed by sintering at a temperature of 1130 °C for 4 h in air atmosphere. X-ray diffraction (XRD) data is obtained in a powder diffractometer (RIGAKU ULTIMA IV, JAPAN) using CuK_α radiation ($\lambda = 1.5405 \text{ \AA}$) with Bragg angles 2θ ranging from 20° to 80° at a scanning rate of $1^\circ/\text{min}$. To know molecular vibrations of the studied sample, Fourier transformed infrared spectroscopy (FTIR) was carried out using a JASCO, Model-FTIR-4100 FTIR spectrometer. The optical band gap was determined from absorbance spectra obtained from UV–Visible (UV–Vis) spectroscopy, by using a SHIMADZU-2600 double beam UV–Vis spectrometer. Raman spectra were collected in the frequency range of $130\text{--}1400 \text{ cm}^{-1}$, using 532 nm excitation solid state diode laser source, a neutral density (ND) filter, TE cooled Solid Czerny–Turner type spectrometer, a high performance UV enhanced state detector and a 50X objective in a microscope. The spectrometer has a focal length of 550 mm with the spectral resolution of 1 cm^{-1} . The microstructure of the gold plated sintered pellet was imaged using Field Emission Scanning Electron Microscope (FESEM) (Carl Zeiss, NTS Ltd., UK), at room temperature. The pellets were polished by sand paper for smoothening its faces and then, silver paint on both surfaces were coated to measure electrical parameters. The moisture was removed by drying the pellets at 150 °C with a duration of 2 h. The dielectric and impedance parameters were recorded in a temperature range 30 °C– 500 °C, at the interval of 5 °C, with frequency variation ranging from 1 kHz to 1 MHz by the help of a LCR meter (PSM 4NL; Model 1735, UK), controlled by computer. The sample holder was designed in our laboratory and a Chromel–Alumel thermo-couple and a digital millivoltmeter (KUSAM MECO 108) was used for monitoring the temperature. A P-E loop tracer (M/S Marine India, New Delhi) was used to trace the PE loop of our poled pellet (electric field 6 kV/cm for a time duration of 8 h) at room temperature. The piezoelectric coefficient (d_{33}) of the studied material was obtained by using Sinoceramics piezo d_{33} test system (Model YE2730A d_{33} METER).

3 Results and discussion

3.1 Structural and microstructural analysis

Figure 1a reflects X-rays diffraction (XRD) patterns of 0.05(KBT)–0.95(NN). The single and sharp diffraction lines indicate that compound is formed, as the lines are different from ingredients. The analysis of this XRD pattern is performed by Rietveld refinement technique, using FullProf Programme [29]. Thomson-Cox-Hasting profile function has been used for the refinement of observed diffraction pattern. The linear interpolation method is adopted here for the suitable background. Other important parameters such as zero correction, displacement, scale factor, background, cell parameters, and Wyckoff positions are also refined. The occupancy of the atomic sites are calculated and kept fixed during refinement. The refined

Rietveld patterns such as R_p , R_{wp} and χ^2 suggest the good fit between experimental and simulated data. All the structural parameters of the sample are reflected in Table 1. However, the refinement becomes reliable by ensuring the parameters i.e. R_{wp} (13.9) and χ^2 (2.324). The fitting between the experimental and simulated data with their difference is well reflected from Fig. 1. From the Rietveld analysis, the studied sample shows an orthorhombic structure with space group $Pmc2_1$, with the lattice parameters, $a = 7.7835$ (8) Å, $b = 5.5132$ (7) Å, $c = 5.5599$ (7) Å and Volume = 238.5877 \AA^3 error bars. From the Scherrer's equation [30],

$$D_{hkl} = \frac{K\lambda}{\beta_{1/2} \cos \theta_{hkl}}, \quad (1)$$

the average particle size (D) of the crystallites is determined as 30 nm. The other terms in Scherrer's equation is defined

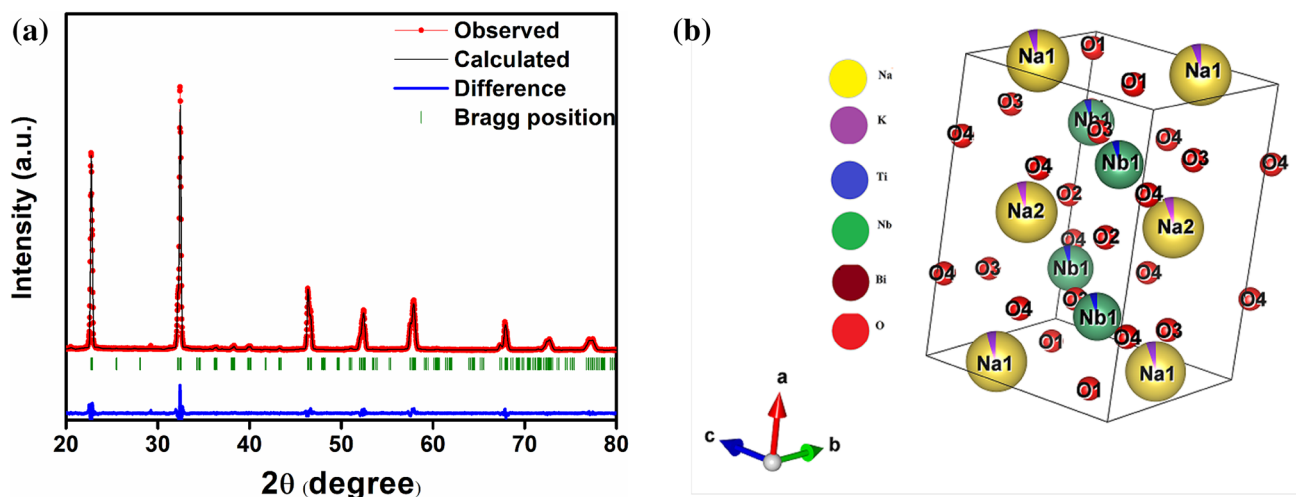


Fig. 1 a, b (XRD) pattern of 0.05($K_{0.5}Bi_{0.5}TiO_3$)-0.95($NaNbO_3$) at room temperature and the unit cell of its crystal structure using VESTA software

Table 1 Rietveld refined parameters of the 0.05($K_{0.5}Bi_{0.5}TiO_3$)-0.95($NaNbO_3$)

Atoms	Positions	x	y	z	B	Occ.
Na1	2a	0.00000	0.22448	0.77156	0.1000	0.47500
Na2	2b	0.50000	0.28065	0.75858	0.1000	0.47500
Nb1	4c	0.74900	0.74781	0.79134	0.1000	0.95000
O1	2a	0.00000	0.29863	0.30778	0.1000	0.50000
O2	2b	0.50000	0.28944	0.33116	0.1000	0.50000
O3	4c	0.22000	0.50503	0.07566	0.1000	1.00000
O4	4c	0.27200	0.94768	0.49986	0.1000	1.00000
K1	2a	0.00000	0.22448	0.77156	0.1000	0.02500
Bi1	2b	0.50000	0.28065	0.75858	0.1000	0.02500
Ti	4c	0.00000	0.74781	0.79134	0.1000	0.05000
Residuals	$R_p = 13.1$	$R_{wp} = 13.9$	$R_{Exp} = 9.12$; $\chi^2 = 2.324$			

as k (constant) = 0.89, $\lambda = 1.5405 \text{ \AA}$, $\beta_{1/2}$ = full width at half maximum (in radians).

Figure 1b represents the unit cell of $0.05\text{K}_{0.5}\text{Bi}_{0.5}\text{TiO}_3$ - 0.95NaNbO_3 using VESTA software.

Figure 2a shows micrograph of FESEM of the studied sample, at room temperature, revealing the homogeneous distribution of grains of different sizes, throughout the sample surface with a very few pores. No microscopic defects appeared in form of cracks or micro cracks are detected. The grain sizes range between 0.5 and 2 μm . The presence of TiO_2 , Bi_2O_3 and Nb_2O_5 in the solid solution dominates the oxygen vacancies which may be responsible to improve grain growth. In present context, the major contribution to oxygen vacancies may be occurred due to volatilization of Bi atoms along with valency fluctuations (Ti^{4+} - Ti^{3+} , Nb^{5+} - Nb^{4+}). The identification of the elements in current investigated system is performed by EDS method. Figure 2b reflects the EDS spectra obtained from the sintered pellet suggests that all the cationic elements are present. The absence of foreign element confirms the purity of the sample.

3.2 Optical properties

3.2.1 Raman spectroscopy

Figure 3 represents Raman spectra of the studied pellet. The fitting to the Raman spectra is carried out by using peak-fit software, which is represented by red line [31] for finding out the FWHM and the peak positions. The Raman modes at 143, 181, 214, 248, 279, 329, 406, 485, 522, 550, 586, 622, 656, 703 and 858 cm^{-1} are observed which are de-convoluted from three Raman modes located at 215.7, 585.7 and 859.3 cm^{-1} . After doping of NaNbO_3 in KBT it is expected that few Nb and Na are placed in

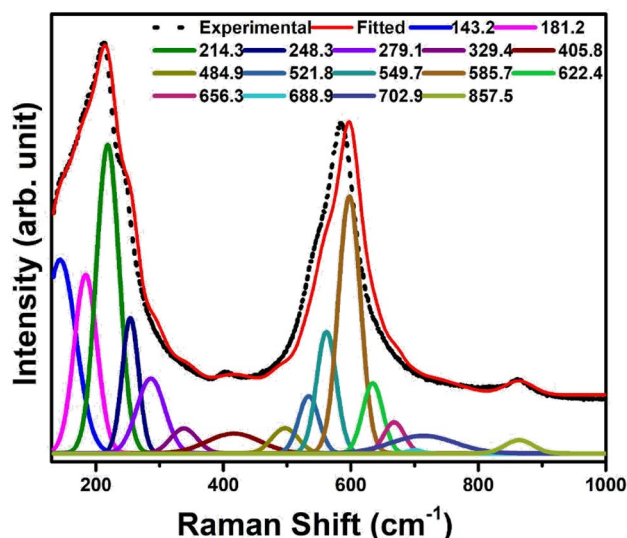


Fig. 3 Raman spectra of $0.05(\text{K}_{0.5}\text{Bi}_{0.5}\text{TiO}_3)$ - $0.95(\text{NaNbO}_3)$

place of K and Bi. The ionic radii of K, Bi are greater than Nb and Na due to their atomic masses. The Raman spectra is affected as compressive stress is developed inside the KBT-NN lattice by doping of NaNbO_3 . From Hou et al. report [32], Raman bands are located at 150, 201, 276, 332, 529 and 633 cm^{-1} which are very close to the our observed Raman mode of 143, 214, 279, 522 and 622 cm^{-1} . These negligible variations are due to the compressive stress caused after doping of Na and Nb. Apart from the above modes, the other bands are correspond to the NN doping. Raman modes below 200 cm^{-1} are related to Bi-O and K-O bonds. In the lower frequency region of 200–300 cm^{-1} , the peaks are characteristics of tetragonal phase of KBT [33]. The crystal structure changes to

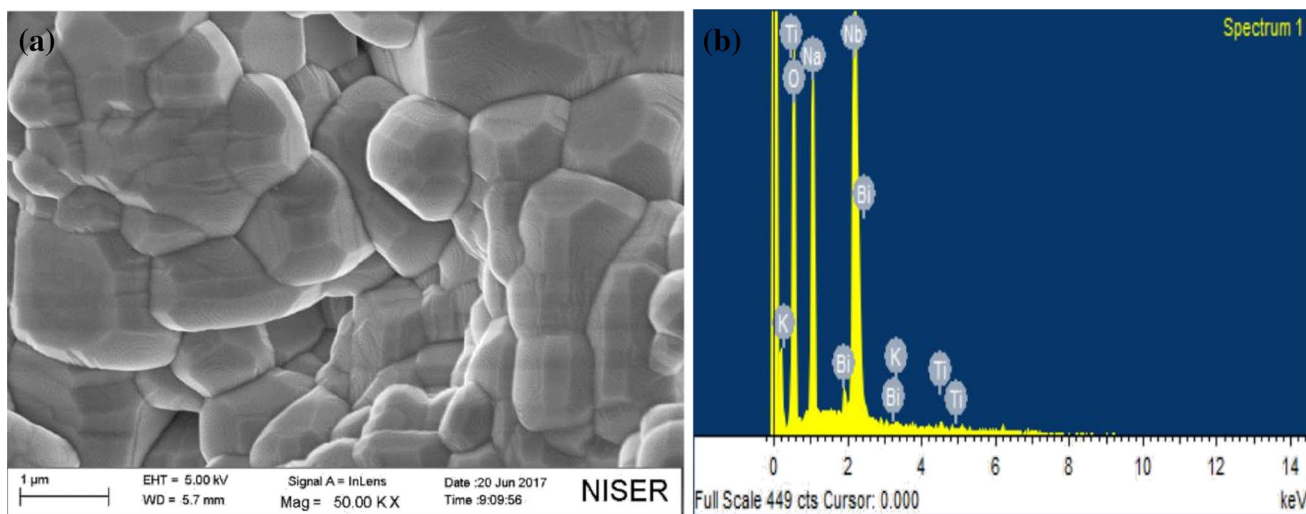


Fig. 2 FE-SEM of $0.05(\text{K}_{0.5}\text{Bi}_{0.5}\text{TiO}_3)$ - $0.95(\text{NaNbO}_3)$

orthorhombic phase after doping with NaNbO_3 . Rusty et al. [34] has been observed band between 800 and 880 i.e. 858 for $\text{Nb}_2\text{O}_5/\text{TiO}_2$ structure which are related to collinear bonds of Nb–O–Nb bands. We observed similar bands in that range at 858 cm^{-1} in the KBT-NN samples of orthorhombic phase and attributed as the Nb–O–Nb related bands. The different position compared to them might be due to the possibilities of Nb_2O_5 structure along with the Na inclusion. The weaker satellite bands exist around the main Raman modes of Nb–Bi, Nb–K, Na–Bi and Na–K bonds due to the Nb–O and Na–O vibrational modes.

3.2.2 FTIR spectroscopy

Figure 4 shows FTIR spectrum of powdered sample. To study the vibrational properties of the sample, FTIR spectroscopy is an important tool. At room temperature FTIR spectra is taken where the wave number ranges from 4000 to 400 cm^{-1} . Three different spectral vibrations are observed at 452, 1142 and 2363 cm^{-1} . The well-defined bands within $900\text{--}400\text{ cm}^{-1}$ are associated with lattice/phonon mode of vibrations identifying the phase of the perovskites [35, 36]. The band 452 cm^{-1} is attributed to vibration of NaNbO_3 frame work including Nb–O stretching, Nb–O–Nb bending and lattice vibrations [35]. The strongest band at 1142 cm^{-1} is attributed to anti symmetric stretching mode of vibration related to oxygen octahedral like NbO_6 , TiO_6 etc. [37]. The small peak at 2363 cm^{-1} is ascribed to both symmetric as well as anti-symmetric mode of vibration.

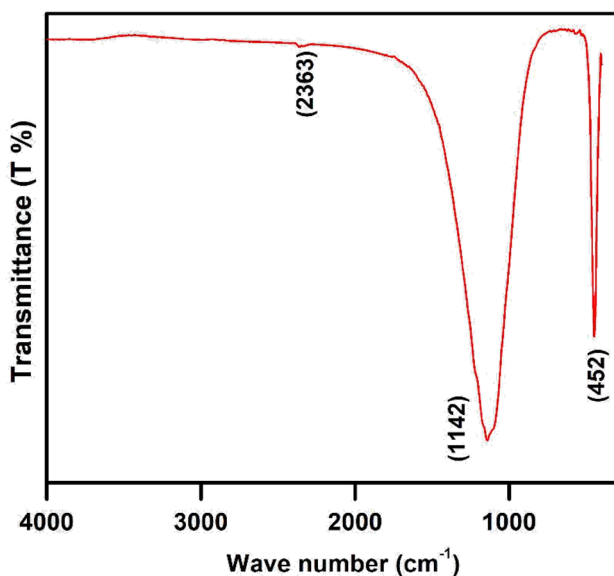


Fig. 4 FTIR spectrum of the $0.05(\text{K}_{0.5}\text{Bi}_{0.5}\text{TiO}_3)\text{--}0.95(\text{NaNbO}_3)$

3.2.3 UV–Vis spectroscopy

Whenever electromagnetic radiation is incident on the sample, it absorbs a part of the radiation leaving the remaining part transmitted. The electrons are excited from occupied valence band to unoccupied conduction band by this absorbed energy by virtue of which the electronic and optical properties of the material can be analyzed. This is known as UV–Vis absorption spectroscopy. By using this analysis, the energy required to overcome band gap in the material can be found out.

3.2.4 Diffuse reflectance and absorbance

In the present study, absorbance A of the material can be measured using the formula $A = -\log_{10} T$, where the transmittance $T = I/I_0$, I and I_0 being the number of photons incident and transmitted. Figure 5a shows that near ultraviolet region, the absorbance of the sample is minimum leading to maximum transmittance, but, the reverse phenomenon is observed in the visible region. The band gap energy can be calculated using the Kubelka–Munk Equation,

$$\alpha E = A(E - E_g)^n, \quad (2)$$

here symbols have their usual meanings. As direct transition is allowed for Perovskites, the value of the index n is taken to be $1/2$. Figure 5b shows the graph of $(\alpha h\nu)^2$ against $h\nu$ [38–40]. The tangent line drawn extrapolating $(\alpha h\nu)^2 = 0$ gives the band-gap energy as 3.2 eV .

3.3 Polarization study

Figure 6 reflects the P–E loop of the material, at room temperature. The remnant polarization is found to be $2P_r = 3.356\text{ }\mu\text{C/cm}^2$ and $E_c = 74.88\text{ kv/c}$ at $30\text{ }^\circ\text{C}$ confirming the ferroelectric behavior of the material. The present material exhibits high conductivity due to volatile nature of bismuth and valency fluctuation (Ti^{4+} to Ti^{3+} and Nb^{5+} to Nb^{4+}). The P–E loop traced is of rounded corner [40]. However, the sample exhibits high conducting behavior as $\tan\delta$ attains high values studied in above section.

3.4 Dielectric study

The dependence of relative permittivity (ϵ_r) and loss tangent ($\tan\delta$) of $0.05(\text{KBT})\text{--}0.95(\text{NN})$ upon temperature at some particular frequencies is represented in Fig. 7a, b. The ϵ_r decreases with increase of frequency which indicates characteristics of dielectric materials. Again, ϵ_r increases to its maximum value (ϵ_{max}) slowly with subsequent rise of temperature and then falls. A dielectric

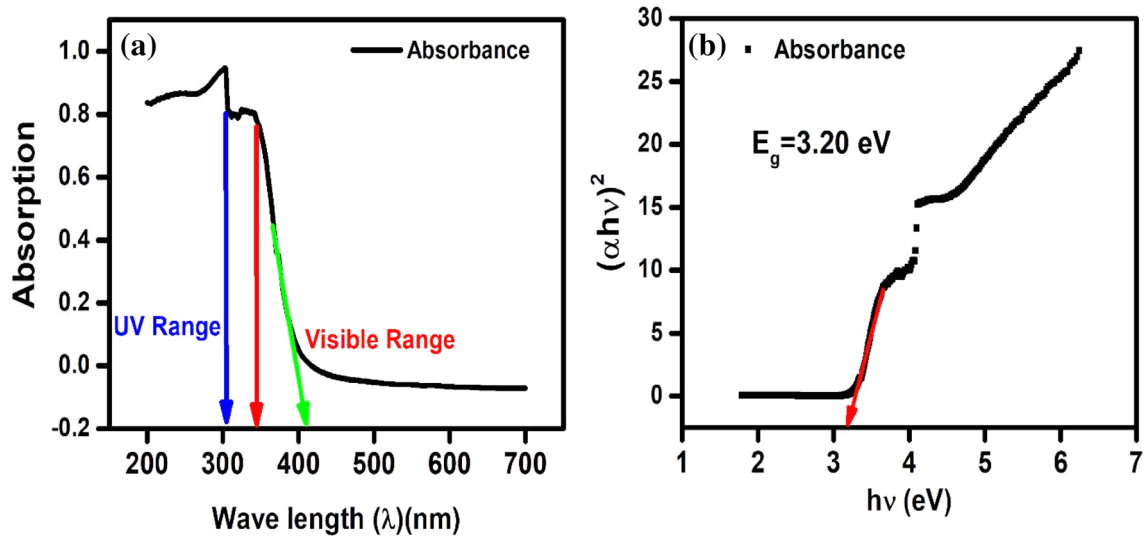


Fig. 5 UV spectra of the $0.05(K_{0.5}Bi_{0.5}TiO_3)-0.95(NaNbO_3)$ for absorbance

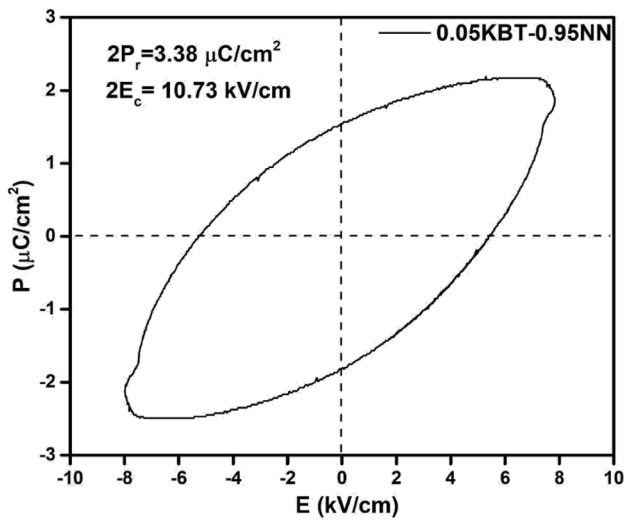
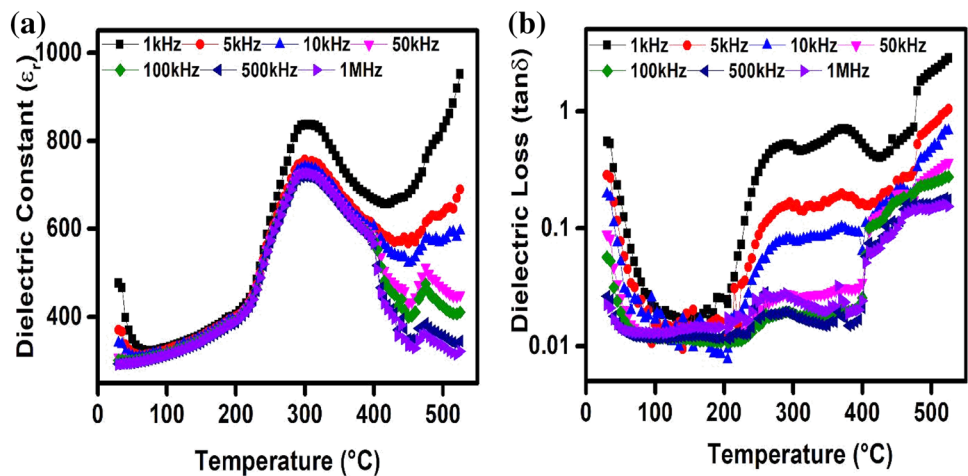


Fig. 6 Hysteresis loop of the $0.05(K_{0.5}Bi_{0.5}TiO_3)-0.95(NaNbO_3)$

Fig. 7 Dielectric constant and dielectric loss vs. temperature at different frequencies of $0.05(K_{0.5}Bi_{0.5}TiO_3)-0.95(NaNbO_3)$



anomaly is observed around $470^{\circ}C$ which corresponds to phase transition of the ferroelectric to paraelectric and is confirmed from P–E loop. Another peak located around $300^{\circ}C$ for all selected frequencies may be attributed to structural phase transition. Beyond the transition temperature, the value of ϵ_r decreases subsequent increase of temperature. The mobility of ions and/or imperfections in the material are responsible for appearance of the space polarization which may be the reason for the further decrease in relative permittivity. The dielectric loss first decreases with increase of temperature, then increases sharply.

3.5 Complex impedance spectroscopy analysis

Complex impedance spectroscopy (CIS) enables us for the characterization of electrical behavior in a ceramic. This technique reflects the response of the material to a sinusoidal disturbance. From the plot of $Z' \sim Z''$, semicircles are

observed. The bulk or grain boundary or interface either alone all a time influences the electrical properties which is inferred from these semicircles. The electrical properties of a material is characterized by the parameters such as complex impedance (Z^*), complex modulus (M^*) and dielectric loss ($\tan\delta$). These parameters are obtained from the relations given below:

Complex impedance

$$Z(\omega) = Z' - jZ'' = R_s - \frac{j}{\omega C_s}, \tag{3}$$

Complex electrical modulus

$$M(\omega) = \frac{1}{\epsilon(\omega)} = M' + jM'' = j\omega C_o Z, \tag{4}$$

here symbols have their usual meanings. The relaxation frequency (ω_{max}) of the bulk material is obtained from the relation:

$$\omega_{max} \tau = \omega_{max} R_b C_b = 1 \Rightarrow \omega_{max} = 1/R_b C_b, \tag{5}$$

where R_b = bulk resistance and C_b = bulk capacitance.

Figure 8 reflects the plot of Z' against frequency at different temperatures of the ceramic. The plot indicates the large values of Z' in low frequency region. But, it decreases monotonously while increasing frequency, for all observed temperatures. The material shows semiconducting behavior as resistance decreases with increase of temperature. The barrier properties reduce as temperature increases which results the increase of the ac conductivity provided that frequency is high [41–43]. In the high frequency region, all the curves merge at one point revealing the independence of Z' from the frequency so also temperature. This is happened due to release of space charge [44].

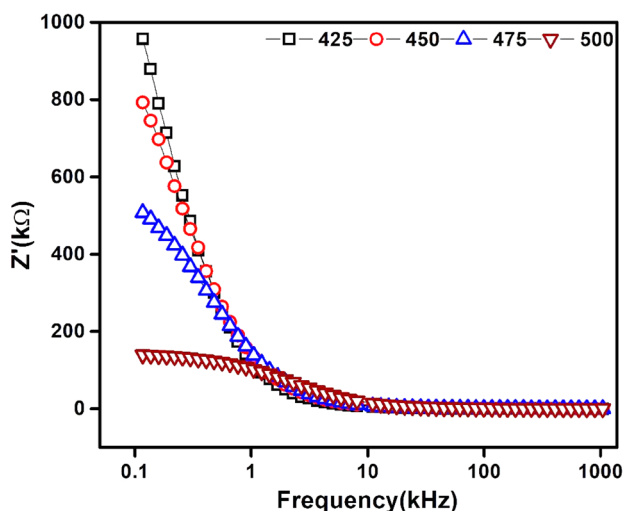


Fig. 8 Variation of Z' with log of frequency of $0.05(K_{0.5}Bi_{0.5}TiO_3)-0.95(NaNbO_3)$ at different temperatures

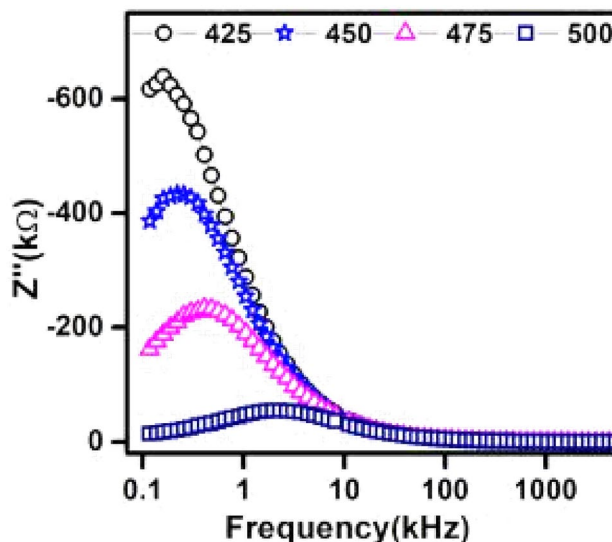


Fig. 9 Variation of Z'' with log of frequency of $0.05(K_{0.5}Bi_{0.5}TiO_3)-0.95(NaNbO_3)$ at different temperatures

Figure 9 represents the graph of the Z'' versus frequency under selected temperatures. The loss spectrum (Z'' vs f) shows relaxation behavior above 250 °C. The type and strength of the electrical relaxation occurred in the material is obtained from the peaks at a particular frequency [45]. The shifting of Z''_{max} towards the higher frequency with rise of temperature indicates the increase of the tangent loss. With increase of temperature, the peaks are broadened indicating the presence of the relaxation in the material which depends upon temperature. In low temperature region, the presence of electrons/immobile species is responsible for relaxation process where as in high temperature region, the responsibility goes to defects/vacancies. The spread of relaxation time with two equilibrium positions is suggested from asymmetric broadening of the peaks. From the plot of $Z'' \sim f$ and using the relation [$Z'' = R_b \{ \omega \tau / (1 + \omega^2 \tau^2) \}$], the proportional of the bulk resistance (R_b) to peak heights is explained. More ever, the monotonous decrease of Z'' high frequencies reveals that space charge is accumulated in these materials [44].

Figure 10 reflects the plot of relaxation time (τ_b) against $1000/T$ validating the Arrhenius relation given by the relation $\tau_b = \tau_o \exp(-E_a/K_B T)$. Here, the symbols carry their own meanings. By fitting the curve linearly, the activation energy is found as 0.41 eV following the aforesaid relation.

Figure 11 shows the Nyquist plots plotted at some temperatures. In low temperature region, the curves are straight lines, inferring the high insulating behavior. As temperature rises, then the curves form semi-circular arcs. The radii of these semi-circular arcs become smaller and smaller with increase of temperature. It results the decrease in the values of bulk resistance. The single semi-circles observed in all the temperatures confirm the effect

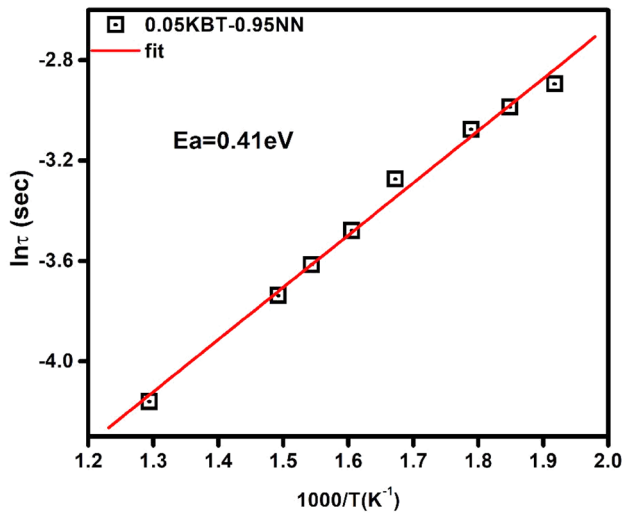


Fig. 10 Variation of relaxation time (τ) as a function of reciprocal of absolute temperature of $0.05(K_{0.5}Bi_{0.5}TiO_3)–0.95(NaNbO_3)$

of grain resistance (bulk property). By using “ZSimpWin” software, the simulation is made with complex impedance data. The equivalent circuit contains one resistor joined in parallel to a constant phase element (CPE). The CPE is given by:

$$Z^*_Q = 1/(i\omega)^n C, \tag{6}$$

here n is a parameter of Jonscher’s power law which does not depend upon frequency. The value of which lies in between 0 and 1. If $n=0$ or 1, then an ideal resistor or an capacitor is represented. The experimental data are well fitted with the simulations made. The fitting parameters for grains (R_g , C_g , n) are imputed in Table 2. As obtained from the fitting parameters, the grain resistances decrease with increase of temperature indicating semiconducting behavior.

Table 2 Comparison of bulk (grain) and grain boundary resistance and capacitance at different temperatures

Temperature (°C)	Rb (in ohm)	Cb (in F)	CPE (Q)	n
250	2.575E6	3.993E–10	5.467E–8	0.24
275	1.584E6	4.665E–10	1.686E–7	0.20
300	1.255E6	5.066E–10	1.349E–9	0.24
350	7.961E5	4.608E–10	7.5E–8	0.26
375	7.053E5	4.28E–10	1.739E–7	0.20
475	5.79E5	1.04E–10	1.637E–9	0.84
500	1.443E5	1.449E–10	3.5331E–9	0.76
525	9.504E4	1.635E–10	8.69E–9	0.68

The resistance and temperature of the material exhibiting semiconducting behavior are related by,

$$R_T = R_N \exp \left[\frac{\beta(T_N - T)}{TT_N} \right], \tag{7}$$

here symbols have their usual meanings. The thermistor characteristic parameter can be expressed as:

$$\beta = \left[\frac{TT_N}{T_N - T} \right] \ln \frac{R_T}{R_N}, \tag{8}$$

The temperature coefficient of resistance (α) is expressed by thermistor parameter β as:

$$\alpha = \left(\frac{1}{R} \right) \left[\frac{d(R)}{dT} \right] = -\frac{\beta}{T^2}, \tag{9}$$

The values of thermistor parameters are imputed in Table 3. The values of β obtained are better than earlier reported data [45–47]. Hence, this high values of β endorse the material for designing thermistor devices.

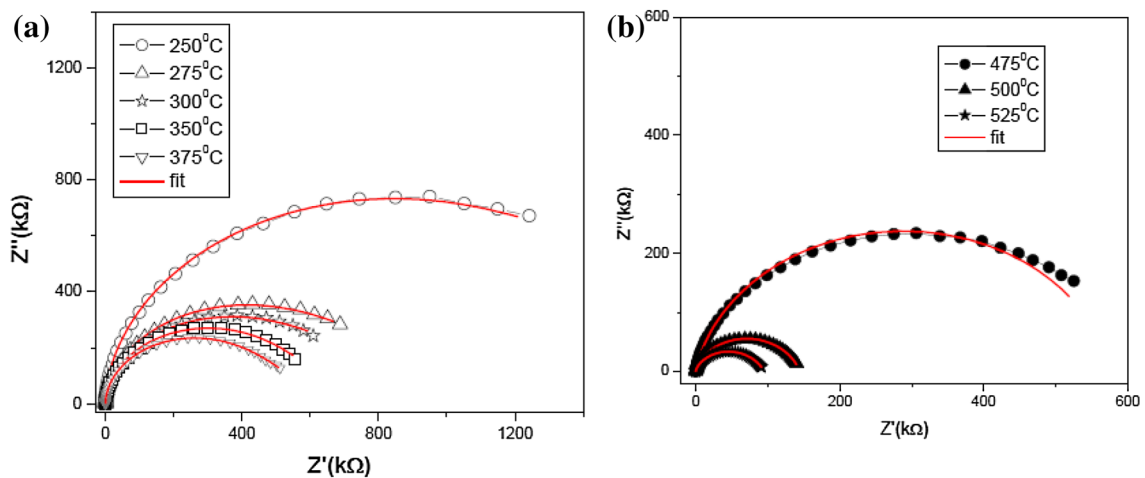


Fig. 11 Variation of Z'' with Z' of $0.05(K_{0.5}Bi_{0.5}TiO_3)–0.95(NaNbO_3)$ at different temperatures (Nyquist Plot)

Table 3 The thermistor parameter α and β for the compound at different temperatures

Temperature (°C)	α	β
250	0.00554	1514
275	0.00529	587
300	0.00506	660
350	0.00465	1805
375	0.00447	878
475	0.00388	2168
500	0.00325	2242
525	0.00364	2315

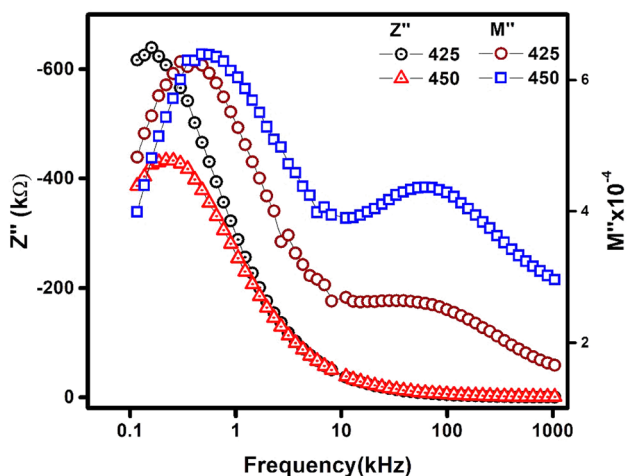


Fig. 12 Variation of M'' and Z'' with frequency at different temperatures of $0.05(K_{0.5}Bi_{0.5}TiO_3)-0.95(NaNbO_3)$

Figure 12 shows the plot of Z'' and $M'' \sim f$. This combined plot detects the presence of the smallest capacitance and the largest resistance as reported by Sinclair et al. [48]. Either short range or long range motion of charge carriers is responsible to cause relaxation process that can be suggested from this plot of Z'' and $M'' \sim f$. When the peaks of Z'' and M'' versus frequency occur at different frequencies, then the relaxation process is caused due to short range motion. The peaks occurring at same frequency is attributed to long range motion [49]. In the studied material, the peaks obtained at different temperatures mismatch suggesting that the short range motion of charge carriers is responsible to cause relaxation process. It is of Non-Debye type [50].

3.6 Complex electric modulus analysis

To differentiate the effect of electrode polarization from grain boundary conduction process and detect bulk properties as apparent with conductivity relaxation times, complex electric modulus technique is adopted [51].

Figure 13a represents the plot of $M' \sim f$ at some selected temperatures. M' becomes nearly zero at lower frequencies. M' attains a maximum asymptotic value with the rise of frequency, for all the selected temperatures. This phenomenon occurs because restoring force is absent. This force governs the mobility of the charge carriers, by applying an induced electric field. It confirms the short range mobility of charge carriers which is already decided from Fig. 11. In high frequency region, M' is constant revealing the fact of absence of electrode polarization [52].

Figure 13b represents the plot of $M'' \sim f$ at some specific temperatures. The observed asymmetric relaxation behavior obtained from this plot suggests that electrical relaxation

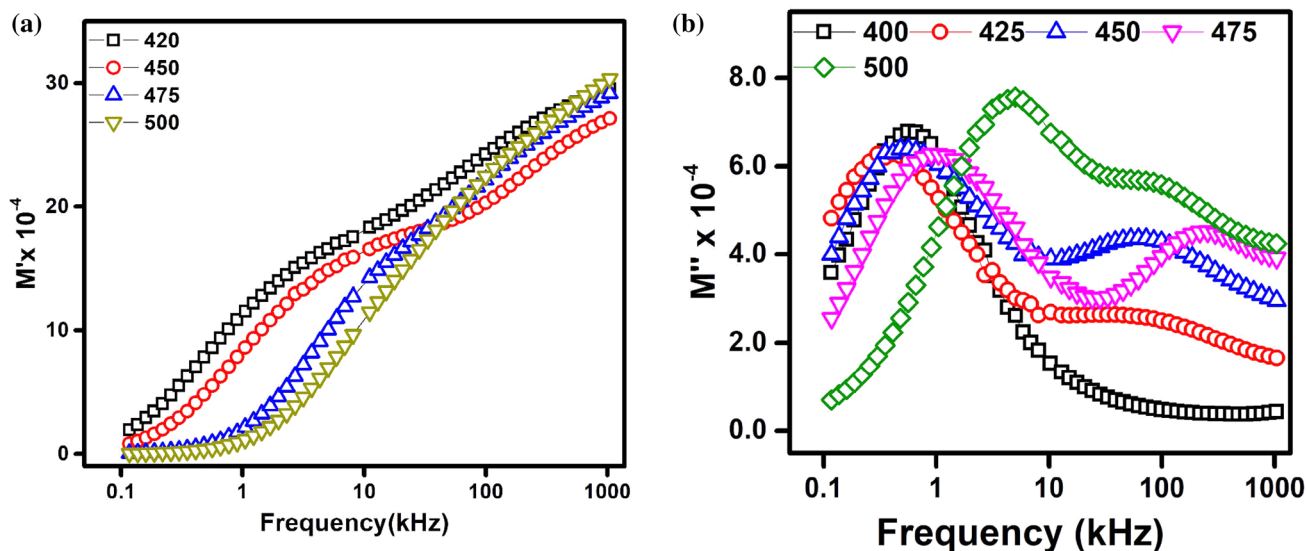


Fig. 13 a, b Variation of M' & M'' with frequency at different temperatures of $0.05(K_{0.5}Bi_{0.5}TiO_3)-0.95(NaNbO_3)$

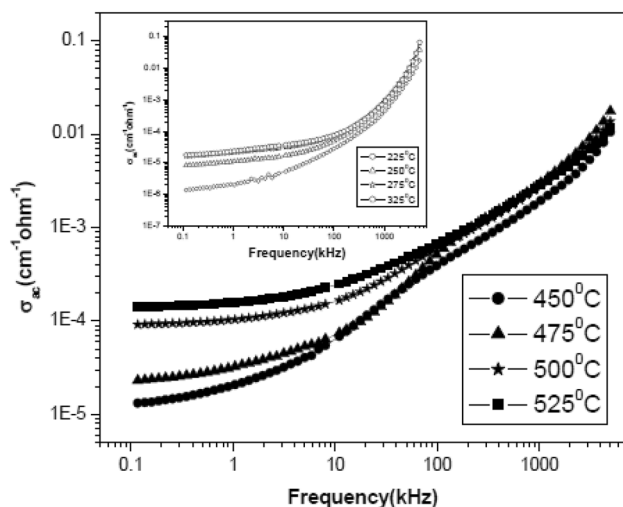


Fig. 14 Variation of σ_{ac} with log of frequency at different temperatures

phenomena in the material is exhibited. Dielectric relaxation is a thermally activated process due to shifting of peaks of M'' towards higher frequency with increase of temperature. Asymmetric broadening of the peak ascribes the spread of relaxation with different time constants which suggests this relaxation in the material is ascribed to be Non-Debye type [53], the same inference is also obtained from Z'' and $M'' \sim f$ plot.

3.7 Ac conductivity analysis

Figure 14 represents the plot of $\sigma_{ac} \sim f$, at some selected temperatures. σ_{ac} is obtained from the empirical formula,

$$\sigma_{ac} = \omega \epsilon_r \epsilon_0 \tan \delta, \quad (10)$$

where the symbols have their usual meanings. Jonscher's power law [50] given by:

$$\sigma_{ac} = \sigma_{dc} + A\omega^n, \quad (11)$$

here n is the frequency exponent which varies from 0 to 1, is well applicable to ac conductivity. As A and n are temperature dependent. The degree of interaction between mobile ions with the lattice around them is represented by n , whereas the strength of the polarizability is represented by A . From this plot, σ_{ac} is nearly independent of frequency, at lower frequencies and increases with rise of frequency. So, σ_{dc} is obtained from the extrapolation of this part towards the lower frequency side. In the high-frequency region, the ac conductivity curves approach each other and increases with increase in frequencies. As $n < 1$, it infers that the hopping process involves translational motion with sudden hopping of charge carriers. The frequency, at where the slope

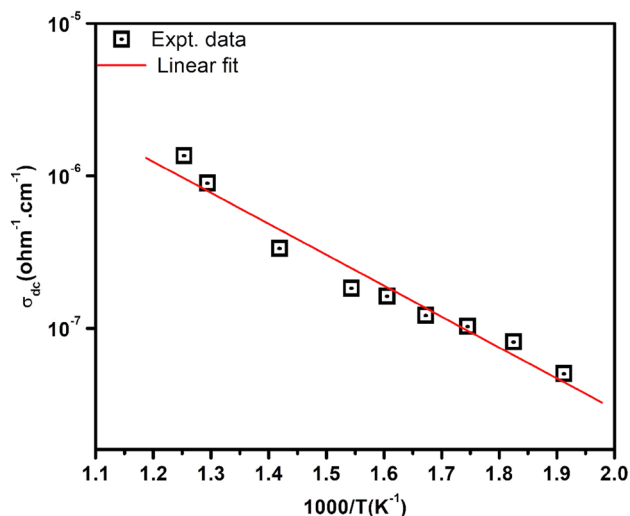


Fig. 15 Variation of σ_{dc} as a function of temperature of $0.05(K_{0.5}Bi_{0.5}TiO_3)-0.95(NaNbO_3)$

changes, is called as the hopping frequency (ω_p) of polaron. It depends on temperature.

3.8 Dc conductivity

Figure 15 represents the plot of dc conductivity with $1000/T$. The dc conductivity is obtained from the formula: $\sigma_{dc} = t/R_b A$, R_b , A and t being bulk resistance, surface area and thickness of the material respectively. Dc conductivity rises with increase of temperature confirming again semiconducting behavior of the material following the Arrhenius relation [51]:

$$\sigma_{dc} = \sigma_0 e^{-\frac{E_a}{k_B T}}. \quad (12)$$

The activation energy obtained is 0.40 eV, nearly same as estimated from the relaxation time plot. This establishes the fact that the conduction so also relaxation in the material occur due to same charge carriers.

4 Conclusions

In summary, we have prepared polycrystalline lead free ceramic $0.05(KBT)-0.95(NN)$ using solid state reaction method and demonstrated its modified structure and superior electrical performance. Our structural studies using FESEM, XRD and Raman spectroscopy have revealed the a homogeneous surface morphology with $0.5-2 \mu m$ and the orthorhombic structure with space group $Pmc2_1$. FTIR investigations has shown the hygroscopic nature of the sample while the Band Gap of 3.2 eV is determined using UV-Vis. Spectroscopy. A phase transition from ferroelectric

to paraelectric material has been inferred from the dielectric and polarization studies. The dc conductivity is found to follow the Arrhenius principle and also confirms semi-conducting behavior of the material. The material exhibits non-Debye type of relaxation as envisaged from complex impedance and modulus analysis. From ac conductivity spectrum, the ceramic is shown to follow Jonscher's universal power law.

Acknowledgements One of the authors H.S.Mohanty acknowledges the financial support from CSIR, India for the SRF fellowship. First author S.K. Mohanty acknowledge the help of Dr. P.K. Sahoo for extending experimental facilities in NISER, Bhubaneswar and UGC for sanctioning Study Leave under FDP programme.

References

1. T. Wang, H. Du, X. Shi, Dielectric and ferroelectric properties of $(1-x)\text{Na}_{0.5}\text{Bi}_{0.5}\text{TiO}_3-x\text{SrTiO}_3$ lead-free piezoceramics system. *J. Phys.* **152**, 012065 (2009)
2. B. Parija, S.K. Rout, L.S. Cavalcante, A.Z. Simões, S. Panigrahi, E. Longo, N.C. Batista, Structure, microstructure and dielectric properties of $100-x(\text{Bi}_{0.5}\text{Na}_{0.5})\text{TiO}_3-x[\text{SrTiO}_3]$, composites ceramics. *Appl. Phys. A* **109**, 715 (2012)
3. M. Rawat, K.L. Yadav, Dielectric, ferroelectric and magneto-electric response in $\text{Ba}_{0.92}(\text{Bi}_{0.5}\text{Na}_{0.5})_{0.08}\text{TiO}_3-\text{Ni}_{0.65}\text{Zn}_{0.35}\text{Fe}_2\text{O}_4$ composite ceramics. *Smart Mater. Struct.* **23**, 085032 (2014)
4. D. White, X. Zhao, M.F. Bresser, X. Tan, Structure and properties of $(1-x)\text{Pb}(\text{Mg}_{1/2}\text{W}_{1/2})\text{O}_3-x\text{Pb}(\text{Zr}_{0.5}\text{Ti}_{0.5})\text{O}_3$ solid solution ceramics. *J. Mater. Sci.* **43**, 5258 (2008)
5. M.D. Maeder, D. Damjanovic, N. Setter, Lead free piezoelectric materials. *J. Electroceram.* **13**, 385 (2004)
6. R. Selvamani, G. Singh, V. Sathe, V.S. Tiwari, P.K. Gupta, Dielectric, structural and Raman studies on $(\text{Na}_{0.5}\text{Bi}_{0.5}\text{TiO}_3)_{(1-x)}(\text{BiCrO}_3)_x$ ceramic. *J. Phys.* **23**, 55901 (2011)
7. C.F. Buhner, Some properties of bismuth perovskites. *J. Chem. Phys.* **36**, 798 (1962)
8. B.K. Barick, K.K. Mishra, A.K. Arora, R.N.P. Choudhary, D.K. Pradhan, Impedance and Raman spectroscopic studies of $(\text{Na}_{0.5}\text{Bi}_{0.5})\text{TiO}_3$. *J. Phys. D: Appl. Phys.* **44**, 355402 (2011)
9. X. Lu, J. Xu, L. Yang, C. Zhou, Y.Y. Zhao, C. Yuan, Q. Li, G. Chen, H. Wang, Energy storage properties of $(\text{Bi}_{0.5}\text{Na}_{0.5})_{0.93}\text{Ba}_{0.07}\text{TiO}_3$ lead-free ceramics modified by La and Zr co-doping. *J. Mater. Sci.* **2**, 87 (2016)
10. Y. Hiruma, R. Aoyagi, H. Nagata, T. Takenaka, Ferroelectric and piezoelectric properties of $(\text{Bi}_{1/2}\text{K}_{1/2})\text{TiO}_3$ ceramics. *Jpn. J. Appl. Phys.* **44**, 5040 (2005)
11. J. Guo, M. Zhu, L. Li, M. Zheng, Y. Hou, Relaxor to ferroelectric crossover in KBT ceramics by prolonged annealing. *J. Alloys. Compd.* **703**, 448 (2017)
12. Y. Hou, M. Zhu, L. Hou, J. Liu, J. Tang, H. Wang, H. Yan, Synthesis and characterization of lead-free $\text{K}_{0.5}\text{Bi}_{0.5}\text{TiO}_3$ ferroelectrics by sol-gel technique. *J. Cryst. Growth* **273**, 500 (2005)
13. W.L. Li, W.P. Cao, D. Xu, W. Wang, W.D. Fei, Phase structure and piezoelectric properties of NBT-KBT-BT ceramics prepared by sol-gel flame synthetic approach. *J. Alloys. Compd.* **613**, 181 (2014)
14. G.A. Babu, R. Subramanyam, I. Bhaumik, S. Ganeshmoorthy, P. Ramasamy, P.K. Gupta, Growth and characterization of undoped and Mn doped lead-free piezoelectric NBT-KBT single crystals. *Mat. Res. Bull.* **53**, 136 (2014)
15. T. Karthik, S. Asthana, Enhanced mechanical and ferroelectric properties through grain size refinement in site specific substituted lead free $\text{Na}_{0.5-x}\text{K}_x\text{Bi}_{0.5}\text{TiO}_3$ ($x = 0-0.10$) ceramics. *Mater. Lett.* **190**, 273 (2017)
16. H. Xie, D. Li Jin, X. Shen, Wang, G. Shen, Morphotropic phase boundary, segregation effect and crystal growth in the NBT-KBT system. *J. Cryst. Growth* **311**, 3626 (2009)
17. X.H. Hao, A review on the dielectric materials for high-energy storage application. *J. Adv. Dielectr.* **3**, 1330001 (2013)
18. B. Jaffe, W.R. Cook, H. Jaffe, *Piezoelectric Ceramics*, (Academic Press, London, 1971), p. 190
19. S. Lanfredi, M.H. Lente, J.A. Eiras, Phase transition at low temperature in NaNbO_3 ceramic. *Appl. Phys. Lett.* **80**, 2731 (2002)
20. S. Tripathi, D. Pandey, S.K. Mirshra, P.S.R. Krishna, Morphotropic phase-boundary-like characteristic in a lead-free and non-ferroelectric $(1-x)\text{NaNbO}_3-x\text{CaTiO}_3$ system. *Phys. Rev. B* **77**, 052104 (2008)
21. T. Zeng, K.W. Kwok, H.L.W. Chan, Ferroelectric and Piezoelectric properties of $\text{Na}_{1-x}\text{Ba}_x\text{Nb}_{1-x}\text{Ti}_x\text{O}_3$ ceramics. *J. Am. Ceram. Soc.* **89**, 2828 (2006)
22. M.T. Benlahrache, N. Benhamla, S. Achour, Dielectric properties of $\text{BaTiO}_3-\text{NaNbO}_3$ composites. *J. Eur. Ceram. Soc.* **24**, 1493 (2004)
23. H. Wu, A. Navrotsky, Y. Su, M.L. Balmer, Perovskite solid solutions along the $\text{NaNbO}_3-\text{SrTiO}_3$ join: phase transitions, formation enthalpies, and implications for general perovskite energetics. *Chem. Mater.* **17**, 1880 (2005)
24. A. Aydi, H. Khemakhem, C. Boudaya, R. Mühl, New ferroelectric and relaxor ceramics in the mixed oxide system $\text{NaNbO}_3-\text{BaSnO}_3$. *Solid State Sci.* **6**, 333 (2004)
25. C. Chaker, W.E. Gharbi, N. Abdelmoula, H. Khemakhem, A. Simon, M. Maglione, Physical properties of the new ceramics in the mixed oxide system $\text{Na}_{1-x}\text{Li}_x\text{Nb}_{1-x}\text{Sb}_x\text{O}_3$. *J. Alloys Compd.* **481**, 305 (2009)
26. D. Lin, K.W. Kwok, Ferroelectric and piezoelectric properties of new $\text{NaNbO}_3-\text{Bi}_{0.5}\text{K}_{0.5}\text{TiO}_3$ lead-free ceramics. *J. Mater. Sci.* **21**, 1060 (2010)
27. J.R. Macdonald, *Impedance Spectroscopy Emphasizing Solid Materials and Systems (Chapter-4)* (Wiley, New York, 1987)
28. A.P. Barranco, M.P.G. Amador, A. Huanosta, R. Valenzuela, Phase transitions in ferrimagnetic and ferroelectric ceramics by Ac measurements *Appl. Phys. Lett.* **73**, 2039 (1998)
29. H.M. Rietveld, A profile refinement method for nuclear and magnetic structures. *J. Appl. Cryst.* **22**, 65-71 (1969)
30. B.D. Cullity, *Elements of X-ray diffraction* (Addison-Wesley Publishing co. Inc., Reading, 1978)
31. <http://www.sigmaplot.co.uk/products/peakfit/peakfit.php>
32. Y. Hou, M. Zhu, L. Hou, J. Liu, J. Tang, H. Wang, H. and Yan, Synthesis and characterization of lead-free $\text{K}_{0.5}\text{Bi}_{0.5}\text{TiO}_3$ ferroelectrics by sol-gel technique. *J. Cryst. Growth* **273**, 500 (2005)
33. Z.S. D-Ling, L.M. Tao, G.Z. Hui, C.G. Bin, W. Xu, C. Jia, Y. Feng, Raman spectroscopic study of ceramic $\text{Sr}_2\text{Bi}_4\text{Ti}_5\text{O}_{18}$. *Chin. Phys.* **15**, 0854 (2006)
34. M. Rusty Pittman, T. Alexies, Bell, Raman studies of the structure of niobium oxide/titanium oxide ($\text{Nb}_2\text{O}_5.\text{TiO}_2$). *J. Phys. Chem.* **97**, 12178 (1993)
35. M.F. Mostafa, S.S. Ata-Allah, A.A.A. Youssef, H.S. Refai, Electric and AC magnetic investigation of the manganites $\text{La}_{0.7}\text{Ca}_{0.3}\text{Mn}_{0.96}\text{In}_{0.04}\text{Al}_{(1-x)0.04}\text{O}_3$; ($0.0 \leq x \leq 1.0$). *J. Magn. Magn. Mat.* **320**, 344 (2008)
36. S. Coste, A. Lecomte, P. Thomas, T. Merle-Mejean, J.C. Champarnaud-Mesjard, Sol-gel synthesis of TeO_2 -based materials using citric acid as hydrolysis modifier. *J. Sol-Gel Sci. Technol.* **41**, 79 (2007)

37. E.A. Perianu, I.A. Gorodea, F. Gheorghiu, A.V. Sandu, A.C. Ianculescu, I. Sandu, A.R. Iordan, M.N. Palamaru, *Rev. Chim.* **62**, 17 (2011)
38. R.L. Frost, J. Yang, Z. Ding, Raman and FTIR spectroscopy of natural oxalates: implications for the evidence of life on Mars. *Chin. Sci. Bull.* **48**, 1844 (2003)
39. B.N. Parida, R.K. Parida, A. Panda, Multi-ferroic and optical spectroscopy properties of $(\text{Bi}_{0.5}\text{Sr}_{0.5})(\text{Fe}_{0.5}\text{Ti}_{0.5})\text{O}_3$ solid solution. *J. Alloys Compd.* **696**, 338–344 (2017)
40. M. Zheng-Zheng, L. Jian-Qing, T. Z-Ming, Q. Yang, Y. Song-Liu, Improved multiferroic properties of La-doped 0.6BiFeO_3 – 0.4SrTiO_3 solid solution ceramics. *Chin. Phys. B* **21**, 107503 (2012)
41. V. Provenzano, L.P. Boesch, V. Volterra, C.T. Moynihan, P.B. Macedo, Electrical relaxation in $\text{Na}_2\text{O}\cdot 3\text{SiO}_2$ glass. *J. Am. Ceram. Soc.* **55**, 492 (1972)
42. H. Jain, C.H. Hsieh, ‘Window’ effect in the analysis of frequency dependence of ionic conductivity. *J. Non-Cryst. Solids* **172**, 1408 (1994)
43. C.K. Suman, K. Prasad, R.N.P. Choudhary, Complex impedance studies on tungsten-bronze electroceramic: $\text{Pb}_2\text{Bi}_3\text{LaTi}_5\text{O}_{18}$. *J. Mater. Sci.* **41**, 369 (2006)
44. S. Chatterjee, P.K. Mahapatra, R.N.P. Choudhary, A.K. Thakur, Complex impedance studies of sodium pyrotungstate – $\text{Na}_2\text{W}_2\text{O}_7$. *Phys. Status Sol.* **201**, 588 (2004)
45. P.R. Das, B. Pati, B.C. Sutar, R.N.P. Choudhary, Electrical properties of complex tungsten bronze ferroelectrics; $\text{Na}_2\text{Pb}_2\text{R}_2\text{W}_2\text{Ti}_4\text{V}_4\text{O}_{30}$ (R = Gd, Eu). *Adv. Mater. Lett.* **3**, 8 (2012)
46. A. Feteira, Negative temperature coefficient Resistance (NTCR) ceramic thermistors: an industrial perspective. *J. Am. Ceram. Soc.* **92**, 967 (2009)
47. R. Sagar, P. Hudge, S. Madolappa, A.C. Kumbharkhane, R.L. Raibagkar, Electrical properties and microwave dielectric behavior of holmium substituted barium zirconium titanate ceramics. *J. Alloys Compd.* **537**, 197 (2012)
48. D.C. Sinclair, A.R. West, Impedance and modulus spectroscopy of semiconducting BaTiO_3 showing positive temperature coefficient of resistance. *J. Appl. Phys.* **66**, 3850 (1989)
49. Z. Imran, M.A. Rafiq, K. Rasool, S.S. Batool, M.M. Hasan, Temperature dependent transport and dielectric properties of cadmium titanate nanofiber mats. *AIP Adv.* **3**, 032146 (2013)
50. S.M. Pilgrim, A.E. Sutherland, S.R. Winzer, Diffuseness as a useful parameter for relaxor ceramics. *J. Am. Ceram. Soc.* **73**, 3122 (1990)
51. P.S. Das, P.K. Chakraborty, B. Behera, R.N.P. Choudhary, Electrical properties of $\text{Li}_2\text{BiV}_5\text{O}_{15}$ ceramics. *Physica B* **395**, 98 (2007)
52. I.M. Hodge, M.D. Ingram, A.R. West, A new method for analysing the a.c. behaviour of polycrystalline solid electrolytes. *J. Electroanal. Chem. Interfacial Electrochem.* **58**, 429 (1975)
53. J.R. Macdonald, Note on the parameterization of the constant-phase admittance element. *Solid State Ionics* **13**, 147 (1984)

Publisher’s Note Springer Nature remains neutral with regard to jurisdictional claims in published maps and institutional affiliations.